JOURNAL OF AIRCRAFT
Vol. 48, No. 3, May–June 2011

Aerodynamic Evaluation of Miniature Trailing-Edge Effectors for Active Rotor Control

Claude G. Matalanis,* Brian E. Wake, and Daniel Opoku
United Technologies Research Center, East Hartford, Connecticut 06108
and
Byung-Young Min, Nandita Yeshala, and Lakshmi Sankar
Georgia Institute of Technology, Atlanta, Georgia 30332

DOI: 10.2514/1.C031191

This work presents progress on a detailed aerodynamic evaluation of miniature trailing-edge effectors for active rotor control. We begin with a two-dimensional computational fluid dynamics study focused on establishing the dependency of miniature trailing-edge effector effectiveness and performance upon basic geometric parameters of a VR-12 airfoil. The computational fluid dynamics study demonstrated that a miniature trailing-edge effector placed at 10% chord upstream of the trailing-edge and sized at approximately 1% chord is capable of delivering moment coefficient increments of approximately ±0.03, or the same moment authority as a 20% chord conventional flap moving ±2.3°. Wind-tunnel experiments were performed on a model blade section equipped with an operational miniature trailing-edge effector in order to validate the steady computational fluid dynamics results, and reasonable agreement was shown. Finally, a small set of three-dimensional unsteady computational fluid dynamics simulations with the prescribed blade motion of a rotor equipped with miniature trailing-edge effectors were performed. Under high-thrust moderate speed conditions, miniature trailing-edge effectors deployed sinusoidally at 4/rev frequency were capable of reducing 4/rev integrated aerodynamic loads in the vertical direction by approximately 80%.

Nomenclature

c = blade chord
C_d = drag coefficient
C_{Fz} = hub normal force coefficient
C_l = lift coefficient
C_m = moment coefficient
f = actuation frequency, Hz
F_z = hub normal force per unit span
h_f = miniature trailing-edge effector height
M = Mach number
R = rotor radius, ft
Re_c = Reynolds number based on chord
U = freestream velocity
V = helicopter flight speed
x = coordinate in chordwise direction
x_f = chordwise miniature trailing-edge effector location
y = coordinate in lateral direction
z = coordinate in vertical direction
α = angle of attack, °
κ = reduced frequency, $\omega c/2U$
Ω = rotor speed, rad/s
ω = oscillation frequency, rad/s
$\varnothing$ = actuation phase shift, °

Introduction

A MINIATURE trailing-edge effector (MITE) is a small tab placed near the trailing-edge of an airfoil on the lower or upper surface oriented perpendicular to the airfoil chord line. MITEs can be rapidly actuated and/or segmented in the spanwise direction in order to quickly change the local section lift, drag, and moment coefficients of a wing or blade. Similar to gurney flaps, they change the effective camber of an airfoil when deployed, and if a good portion of the MITE remains within the airfoil boundary layer, the impact on drag is small [1–4].

MITEs have already shown strong potential for solving a variety of fixed-wing aerodynamic problems, including flutter suppression and wake vortex alleviation [5–8]. Recently, they have also shown potential for solving several problems associated with dynamic stall of rotorcraft blades [9–15]. An array of MITEs deployed successfully on rotorcraft blades could potentially be used for performance enhancement, vibration and noise reduction, increased maneuverability, and automated blade tracking. The main advantage provided by MITEs is that they are fairly small and require little actuation authority to deploy.

Over the last 20 years, a variety of techniques have been investigated with the goal of achieving active rotor control. These include individual blade control, conventional trailing-edge flaps, and blade integral twist control [16–19]. In terms of aerodynamic performance, and with no regard to actuation and mechanical constraints, MITEs tend to generate more drag per unit lift than a conventional flap or an actively twisting blade. With their small size, however, they can be more easily integrated into a rotor blade envelope and require less power to actuate. The smaller actuators reduce the overall and onblade weight increase usually encountered with active rotor control techniques. Thus, the overall system performance with MITEs may be better despite the slight drag increase.

With the ultimate goal of accurately determining the system-level benefits, this work presents an ongoing aerodynamic evaluation of MITEs for active rotor control. The main objective of the work presented here is to determine the amount of aerodynamic authority, which is practically attainable on a VR-12 blade equipped with a variable height MITE, the impact of the MITE on blade performance, and to make a preliminary prediction on how this aerodynamic authority can impact blade loads and rotor performance. Results from a two-dimensional (2-D) computational fluid dynamics (CFD) parametric study, a set of wind-tunnel tests, and a three-dimensional (3-D) unsteady rotor CFD study will be discussed.

Two-Dimensional Computational Fluid Dynamics Parametric Study

A parametric study was conducted to determine the dependence of aerodynamic authority and performance upon the location and size of

---

Received 26 July 2010; revision received 21 November 2010; accepted for publication 7 December 2010.

*claude.matalanis@utrc.utc.com.

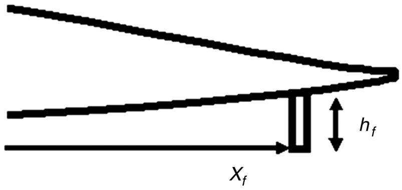

Fig. 1 Schematic diagram of MITE near trailing edge of airfoil illustrating the two primary parameters that were varied in the 2-D CFD study.

the MITE. The VR-12 airfoil was selected for this study. Similar studies have been conducted in the past on different airfoil shapes [4]. This effort was focused not only on evaluating the potential aerodynamic benefits of MITEs but also upon finding a configuration that can be accomplished with a relatively simple mechanical design. Thus, the two main parameters varied were the chordwise location of the MITE x_f and the height of the MITE from the airfoil surface h_f, which are illustrated in Fig. 1. Three MITE locations ($x_f/c = 0.90$, 0.95, and 1.0) and 10 different MITE heights were considered ($h_f/c = \pm 0.0025, \pm 0.005, \pm 0.01, \pm 0.015$, and ± 0.02). We define positive h_f to be on the lower surface. Each case was run at angles of attack between 0 and 14°, in 2° increments.

Several snapshots of the 2-D CFD mesh are shown in Fig. 2. The computational mesh extends 10 chord lengths away from the airfoil in all directions, and it has 497 points about the airfoil surface, 169 points in the direction normal to the airfoil, and 57 points along the MITE in the vertical direction. The minimum cell height normal to the airfoil is $1.0\mathrm{E}-5$ chord lengths. The solver chosen for this study was CFL3-D with the Spalart–Allmaras turbulence model, upwind-biased third-order Roe scheme, and the calculations are steady state. More details on CFL3-D are available in [20]. The freestream Mach number M_∞ was set to 0.2, and the chord-based Reynolds number Re_c was set to approximately $2.0\mathrm{E}+06$ for most cases in order to allow comparison with experiments that were planned for a low-speed wind tunnel. Several cases were run up to a Mach number of 0.6, which confirmed the trends shown at the lower Mach number.

Figure 3 shows plots of lift coefficient versus angle of attack for a representative selection of cases. As expected, greater MITE heights tend to have a larger impact on lift coefficient at all angles of attack before stall, regardless of MITE chordwise location. Also, placing the MITE on the lower surface tends to have a larger effect on lift. This is likely due to larger boundary-layer heights on the upper surface at positive angles of attack, which decrease the momentum of the flow coming into contact with the MITE. As the angle of attack is brought closer to stall, the lift increment due to a MITE on the upper surface is decreased even further. This is due to the small separated region that begins to form on the upper surface near the trailing edge and engulfs the MITE, especially for $x_f/c = 0.95$ and 1.0. For the $x_f/c = 0.90$ case, this effect is not as strong, since the MITE is further upstream and does not become as fully engulfed by the trailing-edge separation. Comparing Figs. 3a–3c carefully indicates that placing the MITE closer to the trailing edge tends to increase the lift increment. This dependency, however, is not as strong as the dependency on MITE height. Note that the lift increments found in this study are very comparable to those found by other researchers. Maughmer and Bramesfeld [15], for example, report lift increments measured experimentally for a similar gurney flap configuration but a very different airfoil shape (S903). The difference in lift increments between the two studies are less than 0.02 for low angles of attack up

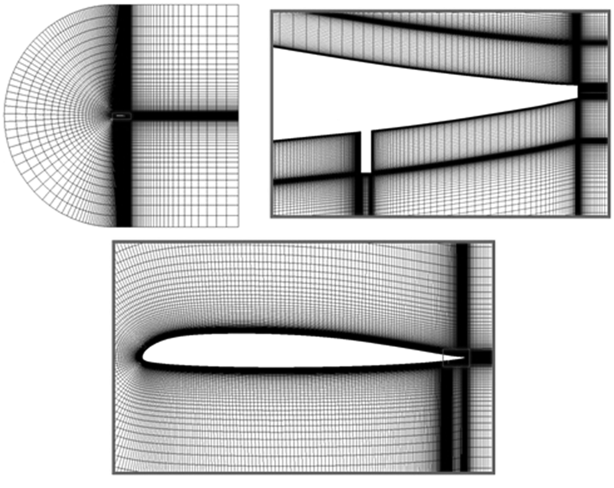

Fig. 2 CFD mesh used for case with MITE height 0.01*c* placed at 0.95*c*.

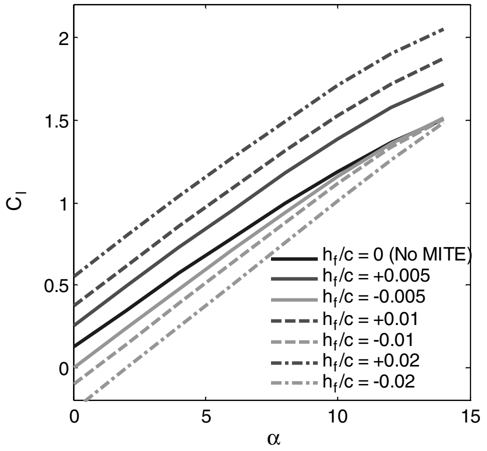

a) $x_f/c = 1.0$

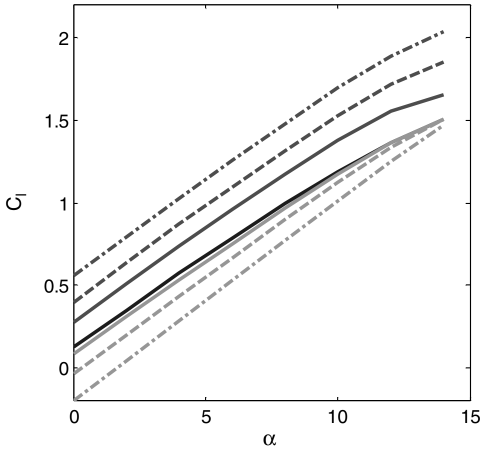

b) $x_f/c = 0.95$

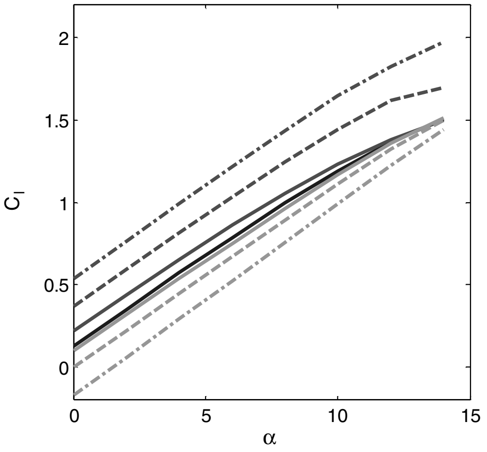

c) $x_f/c = 0.90$

Fig. 3 Lift coefficient plots for select cases with MITE placed at a) $x_f/c = 1.0$, b) $x_f/c = 0.95$, and c) $x_f/c = 0.90$.

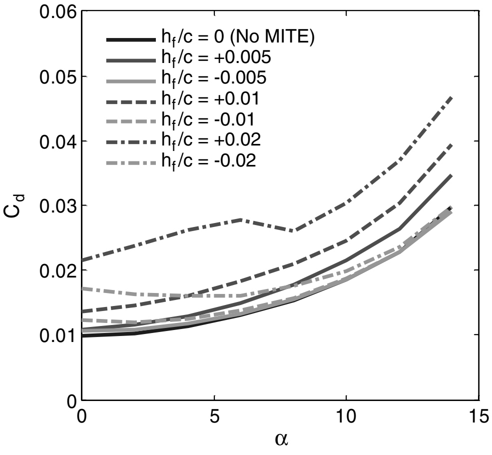

a) $x_f/c = 1.0$

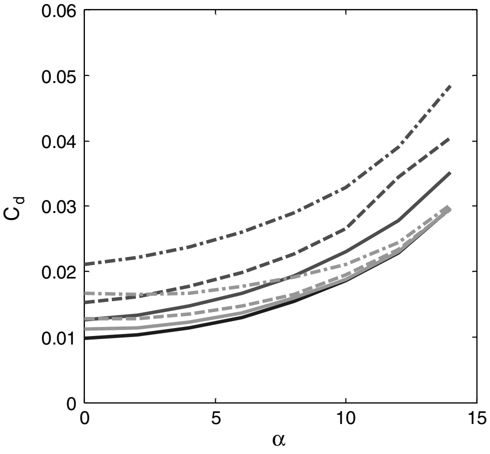

b) $x_f/c = 0.95$

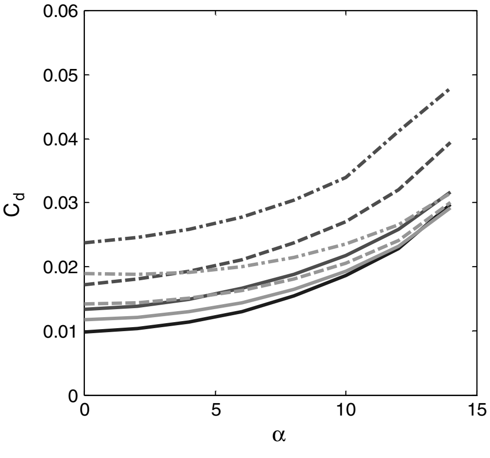

c) $x_f/c = 0.90$

Fig. 4 Drag coefficient plots for select cases with MITE placed at a) $x_f/c = 1.0$, b) $x_f/c = 0.95$, and c) $x_f/c = 0.90$.

to 5°. Differences grow at higher angles of attack due to different stall characteristics of the two airfoils.

Drag results are shown in Fig. 4. It is clear that increasing MITE height at a given angle of attack tends to increase the drag coefficient. The increase is much more pronounced when the MITE is placed on the lower surface, owing once again to the boundary-layer height difference discussed previously. Drag penalty is increased slightly as the MITE is brought further from the trailing edge. This is likely due to the smaller boundary-layer height further from the trailing edge on both the lower and upper surfaces. The $h_f/c = 0.02$, $x_f/c = 1.0$ case shown in Fig. 4a shows heightened levels of drag for $\alpha < 8°$. A closer examination showed that this was due to high-amplitude unsteady shedding immediately downstream of the MITE due to the large size of the MITE and the small boundary-layer height on the lower surface. A small number of time-accurate simulations were run for these cases, which confirmed the presence of unsteady shedding. For consistency, however, the values given here are from the steady simulations; thus, the drag values given for these four points may not be accurate. At $\alpha > 8°$, the shedding subsides. Figure 5 shows lift–drag polars for the same cases. It is clear that most of the drag increment seen in Fig. 4 is due to an increase in lift. Nonetheless, the drag per unit lift is greater for cases with MITEs deployed, which is consistent with previous findings [7–9].

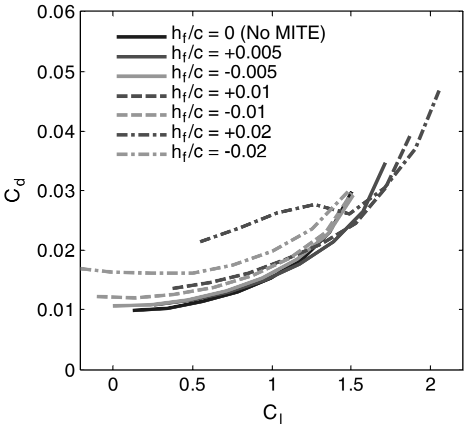

a) $x_f/c = 1.0$

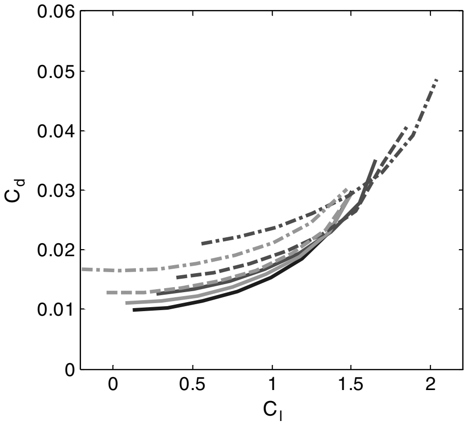

b) $x_f/c = 0.95$

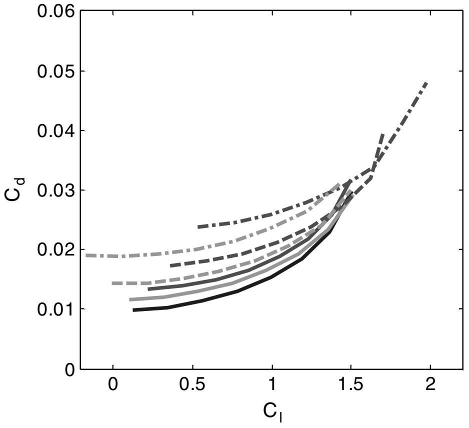

c) $x_f/c = 0.90$

Fig. 5 Lift–drag polars for select cases with MITE placed at a) $x_f/c = 1.0$, b) $x_f/c = 0.95$, and c) $x_f/c = 0.90$.

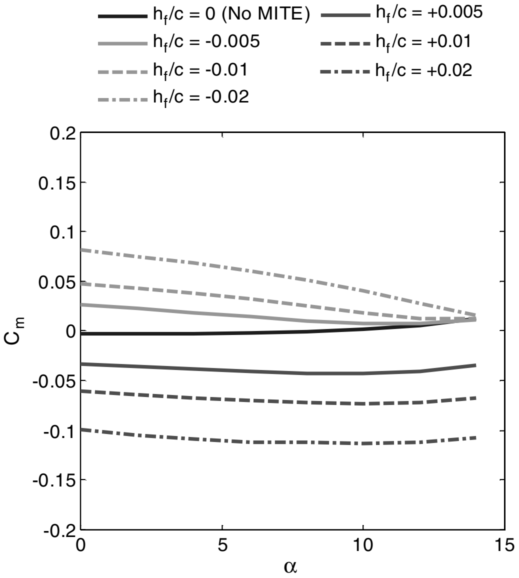

a) $x_f/c = 1.0$

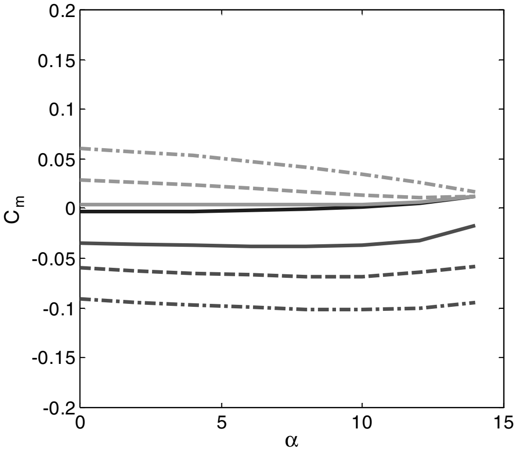

b) $x_f/c = 0.95$

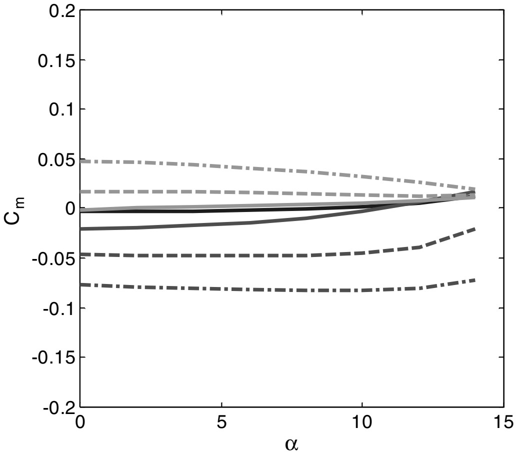

c) $x_f/c = 0.90$

Fig. 6 Moment coefficient plots for select cases with MITE placed at a) $x_f/c = 1.0$, b) $x_f/c = 0.95$, and c) $x_f/c = 0.90$.

Moment coefficients as a function of α are given in Fig. 6. The trends in moment coefficient generally follow the lift coefficient trends previously noted. Figure 7 shows plots of pitching moment coefficient increment C_m evaluated at $\alpha = 0$ as a function of MITE height at the same three chordwise locations as before. This increment is simply defined as the difference between the moment coefficient value at the given configuration and the neutral case moment coefficient. This quantity provides a good measure of aerodynamic authority for rotorcraft applications. Here, we note the same trends that we saw in the lift plots, i.e., asymmetry in effectiveness between upper and lower surfaces and generally greater effectiveness when the MITE is closer to the trailing edge. Furthermore, in Fig. 7a, we see that the moment increment varies in a fairly linear fashion with respect to h_f/c. In Figs. 7b and 7c, however, this is not true. A clear jump in effectiveness occurs between $h_f/c = 0.005$ and 0.01 on the upper surface in Fig. 7b and on both surfaces in Fig. 7c. The reason for this is illustrated by the Mach number contours shown in Fig. 8. When the MITE of $h_f/c = 0.005$ is placed at $x_f/c = 0.95$ for $\alpha = 0$, the flow separation immediately downstream of the MITE fully extends to the airfoil trailing edge. When the same size MITE is placed at $x_f/c = 0.90$, there is sufficient distance downstream of the

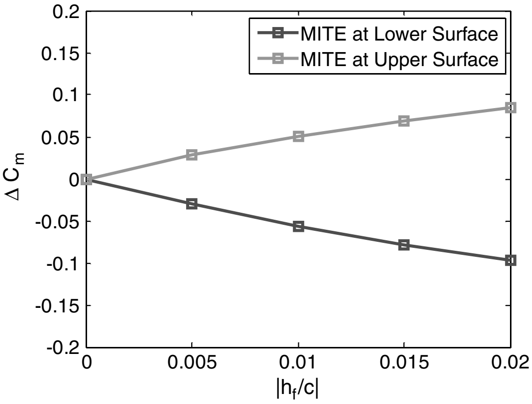

a) $x_f/c = 1.0$

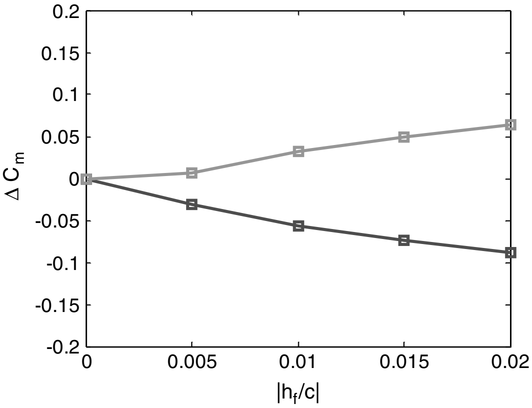

b) $x_f/c = 0.95$

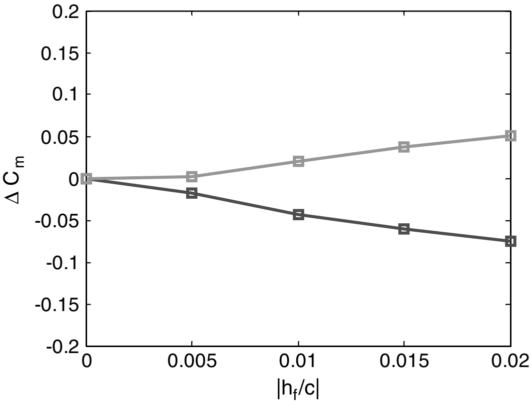

c) $x_f/c = 0.90$

Fig. 7 Moment increment at $\alpha = 0$ as a function of MITE height at a) $x_f/c = 1.0$, b) $x_f/c = 0.95$, and c) $x_f/c = 0.90$.

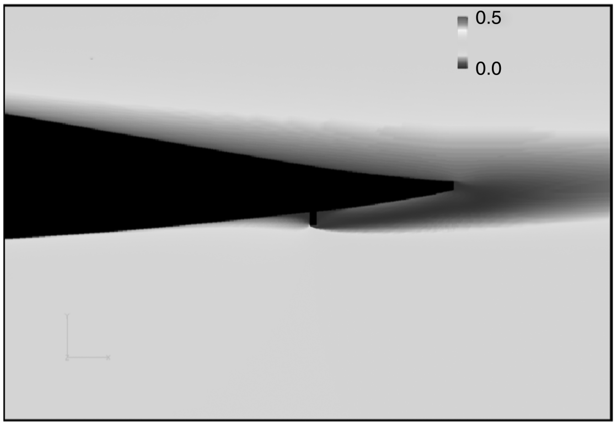

a) $h_f/c = 0.005$, $x_f/c = 0.95$

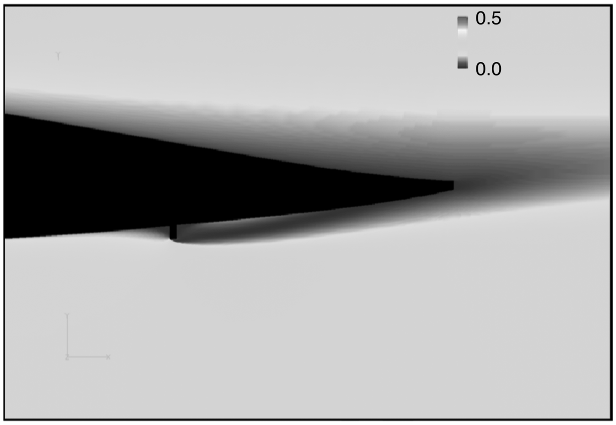

b) $h_f/c = 0.005$, $x_f/c = 0.90$

Fig. 8 Mach number contours for $\alpha = 0$ near the trailing edge for two cases with the same MITE height: a) $x_f/c = 0.95$ and b) $x_f/c = 0.90$. The separated region downstream of the MITE fully extends to the trailing edge in Fig. 8a but begins to attenuate in Fig. 8b.

MITE to allow the flow to begin to reattach. This tends to attenuate the moment authority created by the MITE leading to the nonlinearity seen in Figs. 7b and 7c. This effect has also been noted in [4]. Overall, the most important result of this parametric study is shown by Fig. 7c. Even with the MITE placed at $x_f/c = 0.90$, a reasonable amount of authority is possible with a fairly small MITE. For example, a MITE placed there moving $h_f/c = \pm 0.01$ provides $\Delta C_m \approx \pm 0.03$, which is comparable to the moment authority provided by a 20% chord conventional-size flap moving approximately ±2.3° [19]. The drag coefficient increment is approximately 0.006 with the MITE on the lower surface.

Wind-Tunnel Experiments

Before performing the parametric study discussed in the previous section, a brief validation study was conducted to confirm that the CFD methodology used provided adequate fidelity; however, this study was performed on airfoil shapes different from the VR-12 due to the limited data available at that time. To confirm the results of the parametric study, and examine other phenomena, a set of wind-tunnel experiments on a model VR-12 blade equipped with an operational MITE at $x_f/c = 0.90$ was performed.

The experimental apparatus consisted of a half-span low-aspect-ratio VR-12 blade model, as shown in Fig. 9. An outer shell was fabricated using stereolithography and rigidly supported by a steel strut that connected directly to a six-component loads balance underneath the tunnel test section. The chord length of the model was 17 in., and the half-span was 22 in., giving an overall aspect ratio of approximately 2.6. Three chordwise rows of pressure taps were placed at three points along the span of the airfoil. The points were distributed chordwise, as shown in Fig. 10.

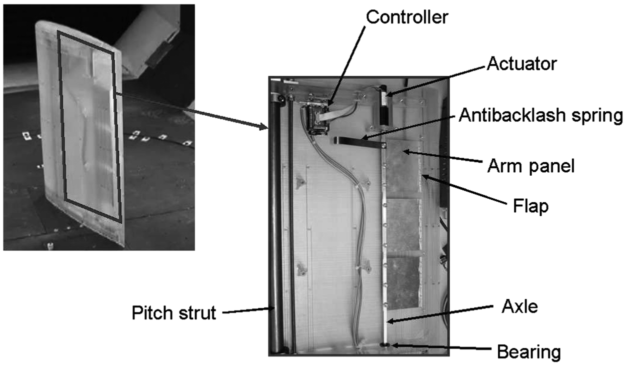

Fig. 9 Half-span model shown mounted in wind tunnel (left) and with pressure side cover removed (right).

These experiments were conducted in the United Technologies Research Center pilot wind tunnel, a low-speed wind tunnel with a maximum speed of approximately 100 mph, and an octagonal 4 × 6 ft test section. All experiments were conducted at approximately $M_\infty = 0.12$ and $Re_c = 1.16\text{E} + 06$. Two sets of experiments were conducted: pressure profiles and loads balance measurements.

Figure 11 shows pressure profile results from the clean airfoil and $h_f/c = -0.015$ for an effective angle of attack of zero, whereby it shows $C_l = 0.127$ for the clean airfoil and -0.095 for the $h_f/c = -0.015$ case. When the MITE is applied on the upper surface, large changes in the pressure distribution occur in three areas: 1) pressure goes up on the upper surface just upstream of the MITE, 2) pressure goes down on the upper surface just downstream of the MITE, and 3) pressure goes down on the lower surface opposite to the MITE. While areas 1 and 3 tend to cause a nose-up pitching moment, area 2 counteracts that effect. This provides a very clear illustration of why MITE effectiveness varies with x_f/c. When the MITE is at the trailing edge, area 2 does not exist; thus, the greatest authority occurs. As we move the MITE away from the trailing edge, area 2 grows in size and influence, causing a decline in effectiveness.

Several corrections were applied to the load balance data in order to facilitate comparison with the 2-D (infinite aspect ratio) CFD results. Because of the low aspect ratio of the experimental model, lift coefficient values were corrected for 3-D effects using the Weissinger method [21]. Next, drag coefficients were corrected by simply subtracting the induced drag term based on an elliptic loading distribution [21]. Finally, lift, drag, and moment coefficients were corrected to account for the fact that the MITE does not span the entire blade. This correction simply involves scaling the increments in each coefficient with the fraction of blade spanned by the MITE. The accuracy of this correction is confirmed in [7,8].

Figure 12 shows a comparison of lift and drag between the CFD and experimental results. Lift coefficients agree very well at low angles of attack where the Weissinger correction is highly applicable. At 12°, however, the agreement breaks down as the 2-D airfoil (CFD) is beginning to approach stall, and the 3-D low-aspect-ratio wing (experiment) remains far from stall. Drag coefficient results did not agree well due to differences in Mach and Reynolds numbers, local wall interference near the root of the model, and uncertainty introduced by the induced drag correction. However, the trends in drag are very comparable, and the most important information required is the change in performance due to MITEs rather than the absolute values. The drag plot in Fig. 12 shows that the increments in performance when the MITE is applied are fairly comparable between experiment and CFD, especially at the lower angles of attack.

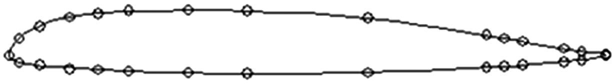

Fig. 10 Chordwise locations of pressure taps at each spanwise station.

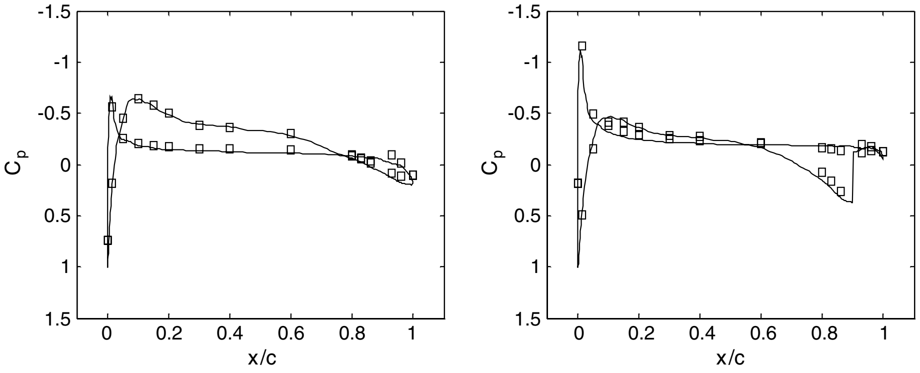

a) b)

Fig. 11 Comparison of pressure coefficient from experiments (symbols) and CFD (lines): a) clean airfoil at $C_l = 0.127$ and b) $h_f/c = -0.015$ at $C_l = -0.095$.

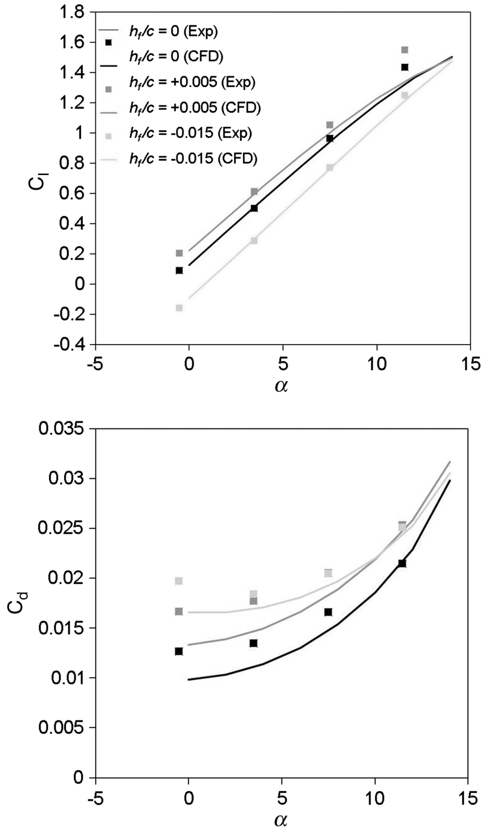

Fig. 12 Comparison of lift and drag coefficients between experiments and 2-D CFD for the clean airfoil and two cases with the MITE deployed.

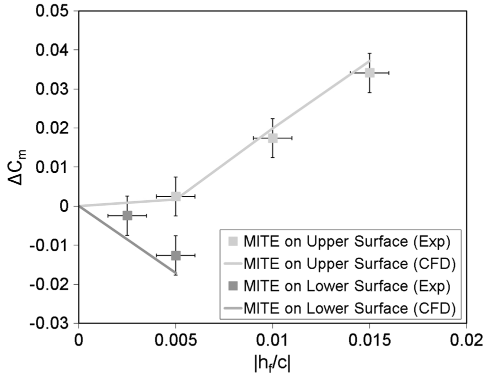

Fig. 13 Moment increments at $\alpha = 0$ for select MITE configurations comparing experiments with the 2-D CFD. Uncertainty bars are based on MITE positioning accuracy, statistical uncertainty, and balance nonlinearity.

The most important result is shown in Fig. 13. Here, we compare the moment increments between the experiments and the CFD. Values are taken at $\alpha = 0$ in order to minimize discrepancies due to 3-D effects. It is clear that the moment increments predicted by the CFD generally fall within the uncertainty of the experimental measurements. This suggests that the MITE configurations examined in this work can indeed provide the levels of aerodynamic authority found in the parametric CFD study.

One final issue was investigated in the wind-tunnel experiments. As shown in Fig. 9, long spanwise slots are present on the lower and upper surfaces of the blade, which allow access for the MITE to deploy. A set of data was collected to determine the potentially negative impact of these slots upon the baseline airfoil performance. Figure 14 shows a lift–drag polar of the $h_f/c = 0$ configuration and the same configuration with the spanwise slots tightly sealed with thin aluminum tape. Since no comparison is made here with 2-D CFD, the results shown in Fig. 14 are uncorrected for 3-D effects (and denoted with uppercase subscripts). Clearly, there is no appreciable degradation in performance due to the slots. Differences in pitching moment were also negligible. Note that the slots used in this experimental model are approximately 0.17 in. in the chordwise direction which is substantially larger than the opening required to allow the MITE to deploy. The reason that the slots have such a minimal effect is likely because, as we saw Fig. 11a, the pressure on the lower and upper surfaces of the clean VR-12 airfoil are very similar. Thus, the amount of flow being driven through the slots would be quite small.

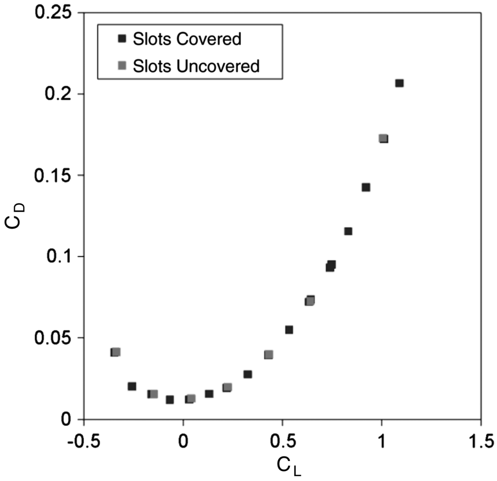

Fig. 14 Comparison of raw (uncorrected) lift–drag polars with spanwise access slots covered and uncovered.

Three-Dimensional Unsteady Simulations

The overall results from the 2-D steady simulations and wind-tunnel experiments suggested that MITEs have enough aerodynamic authority to be used for active rotor control. The goal of the next phase was to quantify the impact of MITEs on a full rotor through a 3-D unsteady simulation.

To simulate the motion of the MITE, a new mesh was constructed for the VR-12 airfoil with a grid-block boundary at $x_f/c = 0.90$ to be used as a variable boundary condition to model an infinitesimally thin MITE. Figure 15 shows a snapshot of the 2-D grid highlighting the variable boundary condition area. Similar to the previous mesh, this mesh extends 15 chord lengths away from the airfoil in all directions, and it has 556 points about the airfoil surface and 140 cells in the direction normal to the airfoil. The minimum cell height normal to the airfoil is $5.0\mathrm{E} - 6$ chord lengths. The wall boundary condition at individual cell faces along this boundary were turned on and off successively at specific times to simulate a moving MITE. The CFD simulations were performed using GENCAS, a generic multiblock unsteady Navier–Stokes solver developed at the Georgia Institute of Technology. These simulations used Roe flux differencing and the Spalart–Allamaras turbulence model. For the full rotor simulations, GENCAS is capable of applying elastic blade motions and performing hybrid Navier–Stokes/free-wake simulations. More details on GENCAS and extensive validation of this unsteady methodology are available in [13,14].

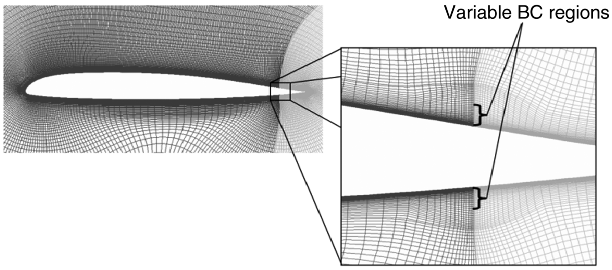

Fig. 15 Grids used for unsteady 2-D simulations with variable boundary condition (BC) technique.

Before the full rotor simulations, several 2-D unsteady cases were run to demonstrate the variable boundary condition technique on the VR-12 geometry. A MITE was simulated at $x_f/c = 0.90$ and oscillated sinusoidally between $h_f/c = \pm 0.01$ at several reduced frequencies with the airfoil $\alpha = 0$ and $M_\infty = 0.628$. The results for unsteady lift, drag, and moment are shown in Figs. 16 and 17. The horizontal lines in the plots show the values for steady-state simulations. As the frequency is increased, the amplitude of lift curves decreases and shows a reduction relative to the steady value. In contrast, the peak values in drag curves increase with frequency, as expected. As the frequency is reduced, the peak values approach the steady-state values. The moment coefficient peaks are unchanged with frequency and are very close to the steady-state values. This behavior of unsteady lift and moment with frequency is consistent with unsteady thin-airfoil aerodynamic theory, in that lift and drag amplitudes change while moment amplitude does not [22].

Despite specifying a smooth sinusoidal MITE motion (in Fig. 16) where no subiterations between time steps are used, small bumps appear in the lift time history, just after the peak values. These bumps were shown to be related to the time accuracy of the simulation. In Fig. 17, a subset of the same cases was run with five subiterations, and these bumps were greatly reduced. The peak values of the lift and moment were not changed; however, the peak value of the unsteady drag did reduce. Of more interest is the mean drag value, and this changed very little (3–4%).

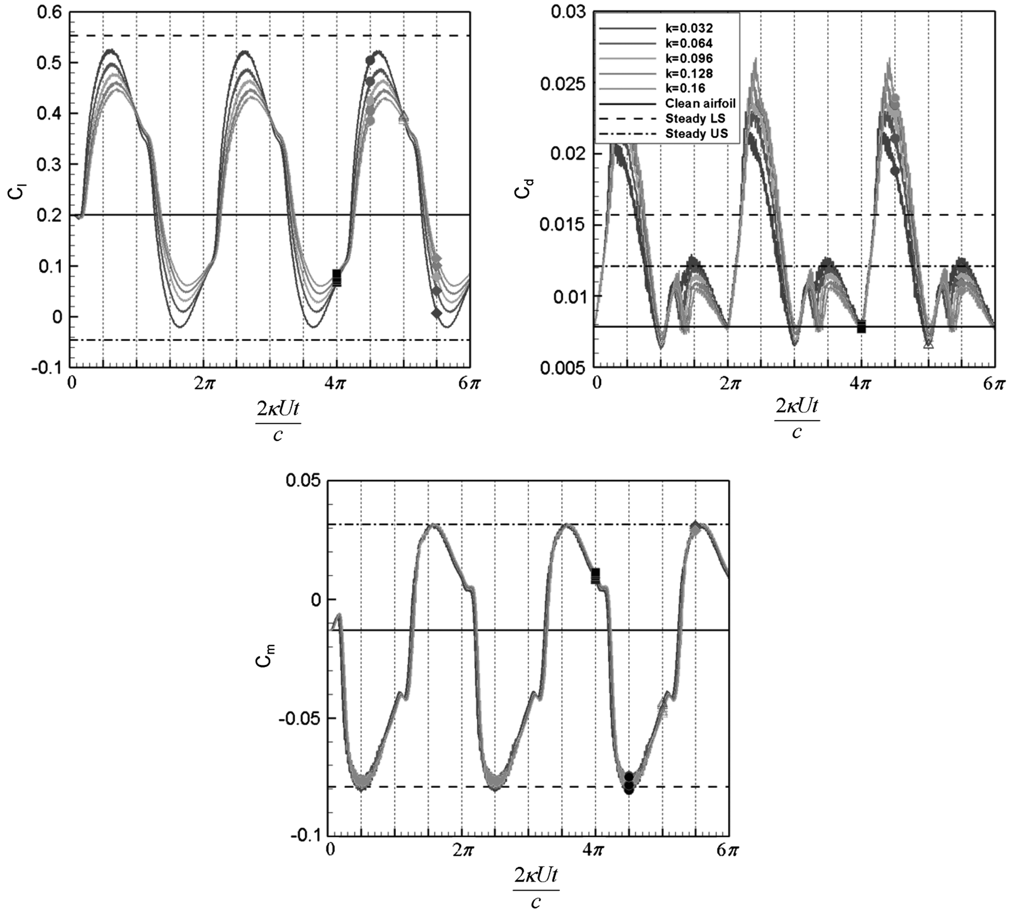

Fig. 16 Lift, drag, and moment coefficients as a function of time for several reduced frequencies of sinusoidal MITE actuation $h_f/c = \pm 0.01$ and $\alpha = 0$, with no subiterations. (LS denotes lower surface and US denotes upper surface.)

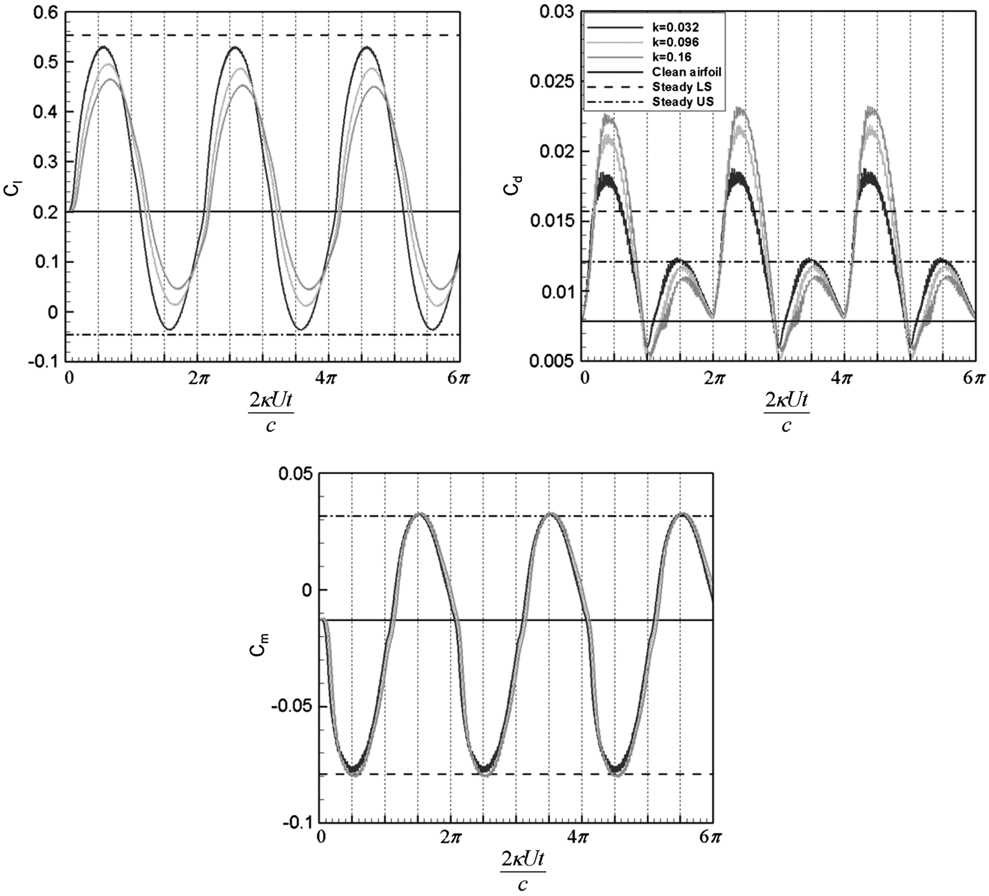

Fig. 17 Lift, drag, and moment coefficients as a function of time for several reduced frequencies of sinusoidal MITE actuation $h_f/c = \pm 0.01$ and $\alpha = 0$, with five subiterations per time step.

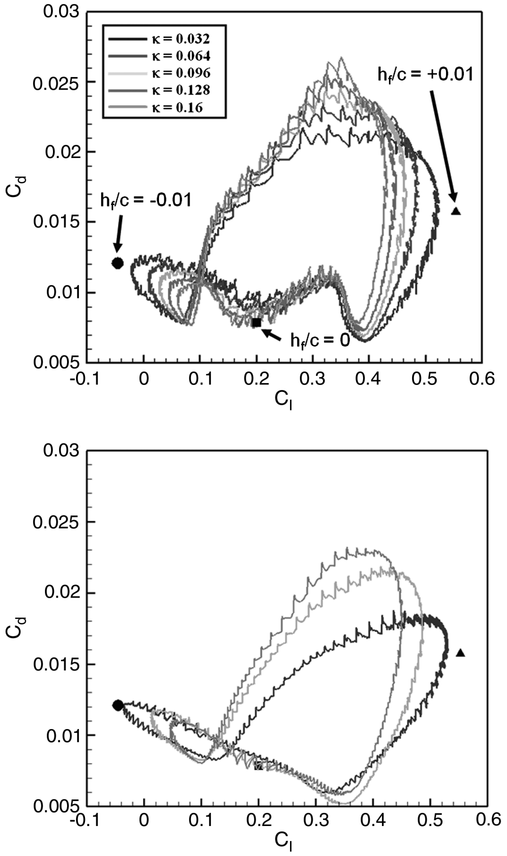

Fig. 18 Lift–drag polars for the same cases shown in Figs. 15 and 16: a) with no subiterations and b) with five subiterations.

Regardless of subiterations, low-amplitude high-frequency oscillations are seen on the drag plots in Figs. 16 and 17. These are due to the discrete nature of the variable boundary condition technique. To examine this more carefully, Fig. 18 shows lift–drag polars of the same results shown in Figs. 16 and 17. The high-frequency oscillations become more apparent when the lift coefficient is varying more rapidly with time, as seen near the highest drag values. Despite these oscillations, none of the simulations performed displayed any unstable behavior. The low-amplitude high-frequency oscillations due to the variable boundary condition technique were

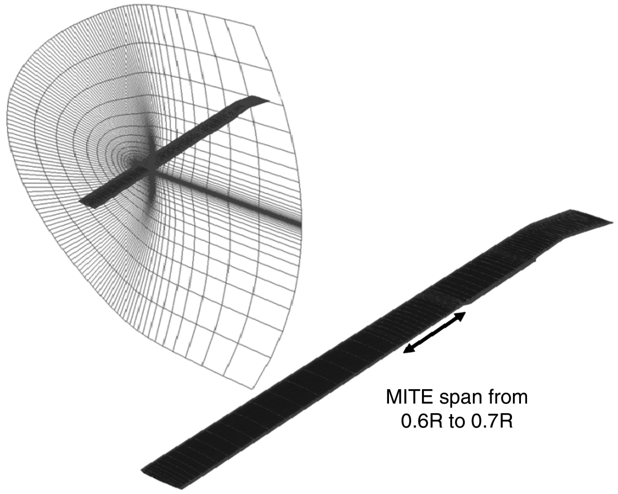

Fig. 19 Images of computational mesh used for 3-D simulations. The UH-60A blade was equipped with an $h_f/c = \pm 0.01$ MITE extending from $0.6R$ to $0.7R$ along the blade span.

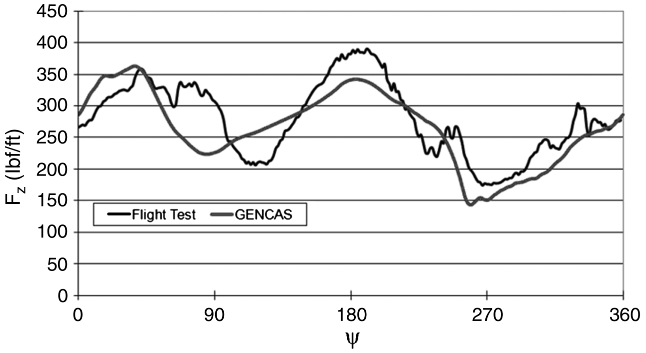

Fig. 20 Comparison of baseline GENCAS simulation to 9017 flight data. GENCAS simulation uses specified blade motions from a converged GT-Hybrid/DYMORE aeroelastic simulation [24].

far outweighed by the relative ease that this technique provided for simulating the MITE motion. If necessary, the magnitude of these oscillations could likely be reduced through grid refinement near the MITE or further modification to the algorithm, such as using an interpolation scheme to provide more continuous updating of the boundary condition.

Finally, several 3-D unsteady hybrid CFD/free-wake rotor simulations were performed using GENCAS. Snapshots of the grid used for these simulations are shown in Fig. 19. This grid has 91 points about the chord of the airfoil, 21 points streamwise along the wake, 45 points normal to the airfoil, and 104 points in the spanwise direction. The minimum cell height normal to the blade is approximately 5.3E − 5 chord lengths. A MITE was placed on each blade across 10% of the rotor radius ($0.6R$ to $0.7R$) and was deployed $h_f/c = \pm 0.01$ sinusoidally at four cycles per revolution. A UH-60A blade geometry was used with one small modification. The portion of the blade spanned by the MITE was replaced with a VR-12 airfoil to be consistent with the previous simulations. A test case showed that this change in the baseline geometry had very little impact on the aerodynamic characteristics of the blade for the conditions considered here. Figure 20 shows a comparison of the integrated aerodynamic loads in the z direction from GENCAS compared with NASA/U.S. Army UH-60A Airloads Program flight counter 9017 data (high-thrust moderate speed; see [23]). Blade motions were specified based on a converged GT-Hybrid/DYMORE simulation (see). The baseline and five cases with different phase shifts were run, as shown in Table 1. The MITE height motion is given by the equation $0.01\sin(2\ \pi \mathrm{ft} - \phi)$, where f corresponded to a 4/rev (4P) actuation frequency. Note that case 4 is a special case where the MITE was actuated only on the lower surface. The integrated aerodynamic loads in the z direction were extracted from the simulation and compiled in Fig. 21. Clearly, there are significant changes in the spectral content of the integrated aerodynamic loads. Most notably, case 5 shows an 80% decrease in 4P content compared with the baseline. Since the blade motions were specified in these simulations, it is not possible to deduce what the change in vibratory loads is; however, this result shows that there is promise that MITEs could be used to reduce 4P rotor vibrations. Full aeroelastic simulations are planned for the next phase of this work, which will provide better indications.

Table 1 Phase shifts of MITE deployment used in the 3-D simulations presented[a]

Case	ϕ, °
1	24.5
2	14
3	0
4	0 (LS)
5	7.5

[a] Case 4 was a special case with MITE deployment on only the lower surface.

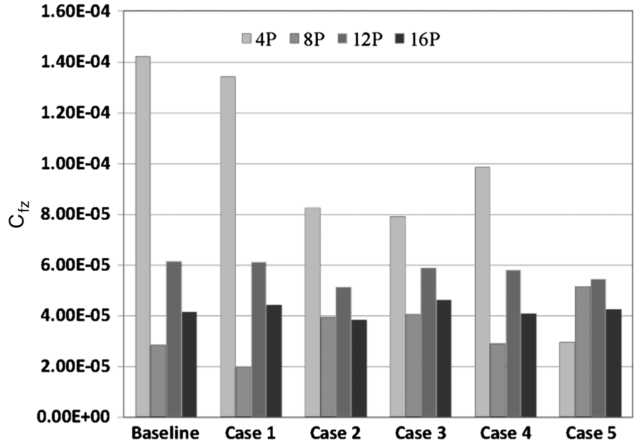

Fig. 21 Spectral amplitudes of integrated aerodynamic loads for the baseline and five phase shifts in $h_f/c = \pm 0.01$ MITE deployment.

Conclusions

The work presented here suggests that MITEs have adequate aerodynamic authority for active rotor control. The results of a 2-D CFD analysis, which was validated through wind-tunnel experiments, indicated that a moment increment of ±0.03 was achievable with a MITE conveniently located 0.10 chords upstream of the trailing edge and actuated to heights of ±0.01 chords. This configuration was applied to 3-D unsteady CFD analysis of a rotor with specified blade motions, which showed that a 4/rev deployment of a MITE with a spanwise length of 0.10 rotor radii can achieve an 80% reduction in 4P integrated aerodynamic loads in the vertical direction. In the next phases of this work, a fully coupled CSD/CFD simulation is planned in order to properly account for the aeroelastic response of the blades.

In addition to aerodynamics, several other factors will ultimately affect the overall benefits that can be achieved with MITEs. As with other active rotor technologies, an appropriate actuator must be designed, suitable feedback and control strategies must be devised, and the overall size and weight of the final design must be minimized. These and other risks must be addressed in future work.

Acknowledgments

The authors gratefully acknowledge the United Technologies Research Center (UTRC) Sikorsky Program for funding this work. Thanks are extended to Jimmy Yeh, Lee Hoffman, and Jim Wicks of UTRC, and Peter Lorber and Alan Egolf of the Sigorsky Program.

References

[1] Myose, R. M., Papadakis, J. K., and Heron, I., "Gurney Flap Experiments on Airfoils, Wings, and Reflection Plane Model," *Journal of Aircraft*, Vol. 35, No. 2, 1998, pp. 206–211.
doi:10.2514/2.2309

[2] Jeffrey, D. R. M., and Hurst. D. W., "Aerodynamics of the Gurney Flap," 14th AIAA Applied Aerodynamics Conference, New Orleans, LA, AIAA Paper 1996-2418, June 1996.

[3] van Dam, C. P., and Yen, D. T., "Gurney Flap Experiments on Airfoils and Wings," *Journal of Aircraft*, Vol. 36, No. 2, March–April 1999, pp. 484–486.
doi:10.2514/2.2461

[4] Baker, J. P., Standish, K. J., and van Dam, C. P., "Two-Dimensional Wind Tunnel and Computational Investigation of a Microtab Modified Airfoil," *Journal of Aircraft*, Vol. 44, No. 2, 2007, pp. 563–572.
doi:10.2514/1.24502

[5] Lee, H.-T., and Kroo, I., "Two Dimensional Unsteady Aerodynamics of Miniature Trailing Edge Effectors," 44th AIAA Aerospace Sciences Meeting and Exhibit, Reno, NV, AIAA Paper 2006-1057, Jan. 2006.

[6] Solovitz, S. A., and Eaton, J. K., "Dynamic Flow Response due to Motion of Partial-Span Gurney-Type Flaps," *AIAA Journal*, Vol. 42, No. 9, 2004, pp. 1729–1736.

doi:10.2514/1.1200

[7] Matalanis, C. G., and Eaton, J. K., "Wake Vortex Alleviation Using Rapidly Actuated Segmented Gurney Flaps," *AIAA Journal*, Vol. 45, No. 8, 2008, pp. 1874–1884.
doi:10.2514/1.28319

[8] Matalanis, C. G., "Wake Vortex Alleviation Using Rapidly Actuated Segmented Gurney Flaps," Ph.D. Dissertation, School of Mechanical Engineering, Stanford Univ., Stanford, CA, Jan. 2007.

[9] Chandrasekhara, M. S., Martin, P. B., and Tung, C., "Compressible Dynamic Stall Performance of a Variable Droop Leading Edge Airfoil with a Gurney Flap," 42nd AIAA Aerospace Science Meeting, Reno, NV, AIAA Paper 2004-0041, 2004.

[10] Kinzel, M. P., Maughmer, M. D., and Lesieutre, G. A., "Miniature Trailing-Edge Effectors for Rotorcraft Performance Enhancement," *Journal of the American Helicopter Society*, Vol. 52, No. 2, April 2007, pp. 146–158.
doi:10.4050/JAHS.52.146

[11] Thiel, M. R., Lesieutre, G. A., Maughmer, M. D., and Koopmann, G. H., "Actuation of an Active Gurney Flap for Rotorcraft Applications," 47th AIAA/ASME/ASCE/AHS/ASC Structures, Structural Dynamics, and Materials Conference, Newport, RI, AIAA Paper 2006-2181, May 2006.

[12] Liu, L., Padthe, A. K., and Friedmann, P. P., "A Computational Study of Microflaps with Application to Vibration Reduction in Helicopter Rotors," 50th AIAA/ASME/ASCE/AHS/ASC Structures, Structural Dynamics, and Materials Conference, Palm Springs, CA, AIAA Paper 2009-2604, May 2009.

[13] Min, B. Y., Sankar, L. N., Rajmohan, N., and Prasad, J. V. R., "Computational Investigation of Gurney Flap Effects on Rotors in Forward Flight," *Journal of Aircraft*, Vol. 46, No. 6, Nov.–Dec. 2009, pp. 1957–1964.
doi:10.2514/1.41918

[14] Min, B. Y., "A Physics Based Investigation of Gurney Flaps for Enhancement of Rotorcraft Flight Characteristics," Ph.D. Dissertation, School of Aerospace Engineering, Georgia Inst. of Technology, Atlanta, GA, May 2010.

[15] Maughmer, M. D., and Bramesfeld, G., "Experimental Investigation of Gurney Flaps," *Journal of Aircraft*, Vol. 45, No. 6, Nov.–Dec. 2008, pp. 2062–2067.
doi:10.2514/1.37050

[16] Roget, B., and Chopra, I., "Closed-Loop Test of a Rotor with Individually Controlled Trailing-Edge Flaps for Vibration Reduction," *Journal of the American Helicopter Society*, Vol. 55, No. 1, 2010, Paper 012009.
doi:10.4050/JAHS.55.012009

[17] Shin, S., and Cesnik, C. E. S., "Helicopter Vibration Reduction in Forward Flight Using Blade Integral Twist Control," 43th AIAA/ASME/ASCE/AHS/ASC Structural Dynamics and Materials Conference, Denver, CO, AIAA Paper 2002-1447, April 2002.

[18] Jacklin, S. A., Haber, A., deSimone, G., Norman, T. R., Kitaplioglu, C., and Shinoda, P., "Full-Scale Wind Tunnel Test of an Individual Blade Control System for a UH-60 Helicopter," *American Helicopter Society 58th Annual Forum*, Montreal, American Helicopter Soc., Alexandria, VA, June 2002.

[19] Chaudhry, Z. A., Wake, B. E., Bagai, A., Lorber, P. F., and Collins, A. J., "Active Rotor Development for Primary and Secondary Flight Control," *American Helicopter Society 65th Annual Forum*, Grapevine, TX, American Helicopter Soc., Alexandria, VA, May 2009.

[20] Krist, S. L., Biedron, R. T., and Rumsey, C. L., "CFL3-D User's Manual (Version 5)," NASA TM 1998-208444, June 1998.

[21] Schlichting, H., and Truckenbrodt, E., *Aerodynamics of the Airplane*, McGraw–Hill, New York1979, pp. 112–153.

[22] Theodorsen, T., "General Theory of Aerodynamic Instability and the Mechanism of Flutter," NACA Rept. 496, Langley Field, VA, May 1934.

[23] Bousman, W. G., and Kufeld, R. M., "UH-60A Airloads Catalog," NASA TM 2005-212827, Aug. 2005.

[24] Rajmohan, N., Manivannan, V., Sankar, L. N., Costello, M., and Bauchau, O., "Development of a Methodology for Coupling Rotorcraft Aeromechanics and Vehicle Dynamics to Study Helicopters in Maneuvering Flight," *AHS 65th Annual Forum*, American Helicopter Soc., Alexandria, VA, May 2009.